Color transparency and short-range correlations in exclusive pion photo- and electroproduction from nuclei

W. Cosyn,* M. C. Martínez,† and J. Ryckebusch
Department of Subatomic and Radiation Physics, Ghent University, Proeftuinstraat 86, B-9000 Gent, Belgium
(Received 26 October 2007; published 7 March 2008)

A relativistic and quantum mechanical framework to compute nuclear transparencies for pion photo- and electroproduction reactions is presented. Final-state interactions for the ejected pions and nucleons are implemented in a relativistic eikonal approach. At sufficiently large ejectile energies, a relativistic Glauber model can be adopted. At lower energies, the framework possesses the flexibility to use relativistic optical potentials. The proposed model can account for the color-transparency (CT) phenomenon and short-range correlations (SRC) in the nucleus. Results are presented for kinematics corresponding to completed and planned experiments at Jefferson Lab. The influence of CT and SRC on the nuclear transparency is studied. Both the SRC and CT mechanisms increase the nuclear transparency. The two mechanisms can be clearly separated, though, as they exhibit a completely different dependence on the hard-scale parameter. The nucleon and pion transparencies as computed in the relativistic Glauber approach are compared with optical-potential and semiclassical calculations. The similarities in the trends and magnitudes of the computed nuclear transparencies indicate that they are not subject to strong model dependences.

DOI: 10.1103/PhysRevC.77.034602 PACS number(s): 25.20.Lj, 25.30.−c, 11.80.La, 13.75.Gx

I. INTRODUCTION

A commonly used variable to map the transition from hadronic to partonic degrees of freedom is the nuclear transparency. For a given reaction process, it is defined as the ratio of the cross section per target nucleon to the one from a free nucleon. Accordingly, the nuclear transparency provides a measure of the attenuation effects of the nuclear medium on the hadrons produced in some reaction. A phenomenon finding its roots in quantum chromodynamics (QCD) is color transparency (CT). It predicts the reduction of final-state interactions (FSI) of the produced hadron with the surrounding nuclear medium at sufficiently high momentum transfer. Thereby, the hadron is created in a pointlike configuration (PLC) and propagates as a color singlet through the nucleus before evolving to the normal hadron state. If CT effects were to appear at a certain energy, the nuclear transparency would be observed to overshoot the predictions from traditional nuclear physics expectations.

Measurements of nuclear transparencies in search of CT have been carried out with the $A(p,2p)$ [1–4] and $A(e,e'p)$ [5–10] reactions, ρ-meson production [11,12], and diffractive dissociation of pions into di-jets [13]. Nuclear transparencies for the pion photoproduction process $\gamma n \to \pi^- p$ in ^{4}He have been measured in Hall A at Jefferson Laboratory (JLab) [14]. A Hall C experiment has extracted the nuclear transparency for the pion electroproduction process $ep \to e'\pi^+ n$ in ^{2}H, ^{12}C, ^{27}Al, ^{63}Cu, and ^{197}Au [15]. Reference [16] reports calculations in a semiclassical model for the latter electroproduction experiment. In Ref. [17], we introduced a relativistic and quantum mechanical model for computing the nuclear transparencies for the pion photoproduction reaction and compared its predictions to the ^{4}He$(\gamma, p\pi^-)$ data and results from a semiclassical model developed by Gao, Holt, and Pandharipande [18]. In this article, we outline the model in more detail and extend it to electroproduction reactions. The intranuclear attenuation that affects the ejectiles (nucleons and pions) is modeled in terms of a relativistic eikonal approach. The bound-state wave functions are obtained from a relativistic mean-field model. At sufficiently small values for the de Broglie wavelength, we use a relativistic version of Glauber multiple-scattering theory. At wavelengths approaching the range of the nucleon-nucleon and pion-nucleon interaction length, the model offers the flexibility to use optical potentials for modeling FSI mechanisms. Short-range correlations (SRC) induce local fluctuations in the nuclear density. These corrections beyond the mean-field approach influence the intranuclear attenuation. The corresponding changes in the nuclear transparencies have been studied in great depth within the context of $A(e,e'p)$ reactions [19–21]. In $A(\gamma, N\pi)$ and $A(e,e'N\pi)$ processes, both the emerging nucleons and pions are subject to these density fluctuations. The SRC are incorporated into our model through the introduction of a well-chosen central correlation function that induces density correlations into the final system. In our procedure, the proper normalization of the wave functions is guaranteed.

Section II of the article presents the formalism used to calculate the nuclear transparencies. A factorized expression for the cross section is derived for $A(\gamma, N\pi)$ (II A) and $A(e,e'N\pi)$ (II B). Next, in Sec. II C the framework for computing the effects stemming from FSI are discussed. Thereby, special attention is paid to a parametrization of the πN scattering parameters that are required in Glauber calculations. In Sec. II D the incorporation of the CT phenomenon and SRC is discussed. The results of our numerical calculations are presented in Sec. III. FSI effects are investigated and transparency results are shown for the pion photo- and

*Wim.Cosyn@UGent.be
†Present address: Dpto FAMN, Universidad Complutense de Madrid, E-28040 Madrid, Spain.

electroproduction reactions from various target nuclei. Our conclusions are stated in Sec. IV.

II. FORMALISM

In this section, the formalism used to describe $A(\gamma, N\pi)$ and $A(e, e'N\pi)$ reactions is presented.

A. Pion photoproduction

We use the following notations for the four-momenta in the laboratory frame: $q^\mu(q, \vec{q})$ for the photon, $P_A^\mu(E_A, \vec{p}_A = \vec{0})$ for the target nucleus, $P_{A-1}^\mu(E_{A-1}, \vec{p}_{A-1})$ for the residual nucleus, and $P_N^\mu(E_N, \vec{p}_N)$ and $P_\pi^\mu(E_\pi, \vec{p}_\pi)$ for the ejected nucleon and pion. The missing momentum $\vec{p}_m$ is defined as $\vec{p}_m \equiv -\vec{p}_{A-1} = \vec{p}_N + \vec{p}_\pi - \vec{q}$ and the outgoing nucleon has spin m_s. The fivefold differential cross section in the laboratory frame reads

$$\frac{d^5\sigma}{dE_\pi d\Omega_\pi d\Omega_N} = \frac{M_{A-1} m_N p_\pi p_N}{4(2\pi)^5 q E_A} f_{\rm rec}^{-1} \overline{\sum_{fi}} \left|\mathcal{M}_{fi}^{(\gamma,N\pi)}\right|^2, \quad (1)$$

where $\overline{\sum}_{fi}$ involves an averaging over the photon polarizations and a summation over the spins of the final particles. The recoil factor $f_{\rm rec}$ is given by

$$f_{\rm rec} = \frac{E_{A-1}}{E_A}\left|1 + \frac{E_N}{E_{A-1}}\left[1 + \frac{(\vec{p}_\pi - \vec{q})\cdot\vec{p}_N}{p_N^2}\right]\right|, \quad (2)$$

and $\mathcal{M}_{fi}^{(\gamma,N\pi)}$ denotes the invariant matrix element:

$$\mathcal{M}_{fi}^{(\gamma,N\pi)} = \langle P_\pi^\mu, P_N^\mu m_s, P_{A-1}^\mu J_R M_R | \hat{\mathcal{O}} | q^\mu, P_A^\mu 0^+\rangle, \quad (3)$$

where $J_R M_R$ are the quantum numbers of the residual nucleus. We restrict ourselves to processes with an even-even target nucleus A.

The wave functions for the bound nucleons are constructed in an independent particle model (IPM). We use relativistic wave functions from the Hartree approximation to the Walecka model with the W1 parametrization [22]. For the sake of conciseness, only the spatial coordinates of the nucleons are written throughout this work. The single-particle wave functions ϕ_α adopt the following form for a spherically symmetric nuclear potential [23]:

$$\phi_\alpha(\vec{r}) \equiv \phi_{n\kappa m}(\vec{r}, \vec{\sigma}) = \begin{bmatrix} i\frac{G_{n\kappa}(r)}{r}\mathcal{Y}_{\kappa m}(\Omega, \vec{\sigma}) \\ -\frac{F_{n\kappa}(r)}{r}\mathcal{Y}_{-\kappa m}(\Omega, \vec{\sigma}) \end{bmatrix}. \quad (4)$$

Here, n is the principal quantum number and κ and m denote the generalized angular momentum quantum numbers. The spin spherical harmonics $\mathcal{Y}_{\pm\kappa m}$ are defined as:

$$\begin{aligned} \mathcal{Y}_{\kappa m}(\Omega, \vec{\sigma}) &= \sum_{m_l m_s}\left\langle l m_l \ \tfrac{1}{2} m_s \middle| \ jm\right\rangle Y_{l m_l}(\Omega)\chi_{\frac{1}{2}m_s}(\vec{\sigma}), \\ \mathcal{Y}_{-\kappa m}(\Omega, \vec{\sigma}) &= \sum_{m_l m_s}\left\langle \bar{l} m_l \ \tfrac{1}{2} m_s \middle| \ jm\right\rangle Y_{\bar{l} m_l}(\Omega)\chi_{\frac{1}{2}m_s}(\vec{\sigma}), \end{aligned} \quad (5)$$

with

$$j = |\kappa| - \tfrac{1}{2}, \quad l = \begin{cases} \kappa, & \kappa > 0 \\ -\kappa - 1, & \kappa < 0 \end{cases}, \quad \bar{l} = \begin{cases} \kappa - 1, & \kappa > 0 \\ -\kappa, & \kappa < 0 \end{cases}.$$

The ground-state wave function of the target nucleus $|P_A^\mu 0^+\rangle \equiv \psi_A^{\rm g.s.}(\vec{r}_1, \ldots, \vec{r}_A)$ is obtained by fully antisymmetrizing the product of the individual nucleon wave functions ϕ_α. We model the pion photoproduction process by means of a contact interaction: the initial nucleon, impinging photon, and the ejected pion and nucleon join in a single space-time vertex. As the process can take place on any of the nucleons in the target nucleus, we get the following general expression for the corresponding photoproduction operator:

$$\hat{\mathcal{O}} = \sum_{i=1}^{A} O_\mu(\vec{r}_i). \quad (6)$$

We assume that $\hat{\mathcal{O}}$ is exempted from medium effects. This is a common assumption in nuclear and hadronic physics and is usually referred to as the impulse or quasifree approximation (IA). In the context of $A(e, e'p)$ reaction, for example, the impulse approximation provides a fair description of the data [24]. It is also applied in the experimental analysis of Ref. [15] and the model of Ref. [25]. The impinging photon with polarization λ is represented by

$$A^\mu(\lambda, \vec{r}_i) = \epsilon^\mu(\lambda)\, e^{i\vec{q}\cdot\vec{r}_i}. \quad (7)$$

Here, $\epsilon^\mu(\lambda)$ is the polarization four-vector of the photon. The wave function of the ejected nucleon is written as

$$\begin{aligned} \left|P_N^\mu m_s\right\rangle \equiv \psi^{(+)}_{\vec{p}_N, m_s}(\vec{r}_i) &= \hat{\mathcal{S}}^\dagger_{N'N}(\vec{r}_i; \vec{r}_1, \ldots, \vec{r}_{j\neq i}, \ldots, \vec{r}_A) \\ &\times u(\vec{p}_N, m_s) e^{i\vec{p}_N\cdot\vec{r}_i}, \end{aligned} \quad (8)$$

which is the product of a positive-energy Dirac plane wave $\phi_{\vec{p}_N}(\vec{r}_i) = u(\vec{p}_N, m_s)e^{i\vec{p}_N\cdot\vec{r}_i}$ and an operator $\hat{\mathcal{S}}^\dagger_{N'N}$. This operator describes the attenuation of the ejected nucleon through soft final-state interactions with the other nucleons. The wave function for the ejected pion adopts a similar form as the nucleon one, i.e., a plane wave convoluted with a FSI factor $\hat{\mathcal{S}}^\dagger_{\pi N}$:

$$\left|P_\pi^\mu\right\rangle \equiv \Phi^{(+)}_{\vec{p}_\pi}(\vec{r}_i) = \hat{\mathcal{S}}^\dagger_{\pi N}(\vec{r}_i; \vec{r}_1, \ldots, \vec{r}_{j\neq i}, \ldots, \vec{r}_A) e^{i\vec{p}_\pi\cdot\vec{r}_i}. \quad (9)$$

The final A-nucleon wave function is constructed by antisymmetrizing $\psi^{(+)}_{\vec{p}_N, m_s}$ with the wave function for the residual nucleus $\psi_{A-1}^{J_R, m_R}$:

$$\begin{aligned} \left|P_N^\mu m_s, P_{A-1}^\mu J_R M_R\right\rangle &\equiv \psi_A^{\vec{p}_N, m_s}(\vec{r}_1, \ldots, \vec{r}_A) \\ &= \hat{\mathcal{A}}\big[\hat{\mathcal{S}}^\dagger_{N'N}(\vec{r}_1; \vec{r}_2, \ldots, \vec{r}_A) u(\vec{p}_N, m_s) e^{i\vec{p}_N\cdot\vec{r}_1} \\ &\times \psi_{A-1}^{J_R, m_R}(\vec{r}_2, \ldots, \vec{r}_A)\big]. \end{aligned} \quad (10)$$

As $\psi_A^{\rm g.s.}$ and $\psi_A^{\vec{p}_N, m_s}$ are fully antisymmetric, each term of the operator (6) will yield the same contribution to the matrix element (3) and we can restrict ourselves to the term with coordinate $\vec{r}_1$ and multiply it with A. With the above expressions for the operator and the wave functions of the hadrons involved in the reaction, we can write for the matrix

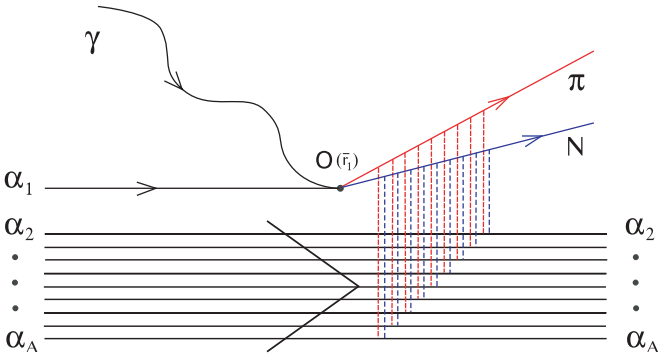

FIG. 1. (Color online) Diagram included in computing the matrix element of Eq. (11). The dashed lines denote the FSI of the ejected pion (red) and nucleon (blue) with the spectator residual nucleons. The diagram shown here is representative for the spectator approximation: one active nucleon N and π are subject to soft collisions with frozen spectator nucleons that occupy the single-particle levels $\alpha_2, \alpha_3, \ldots, \alpha_A$ and are not subject to changes in their quantum numbers.

element of Eq. (3) in coordinate space:

$$\mathcal{M}_{fi}^{(\gamma,N\pi)} = A \int d\vec{r}_1 \int d\vec{r}_2 \ldots \int d\vec{r}_A \times \left[\psi_A^{\vec{p}_N,m_s}(\vec{r}_1,\vec{r}_2,\ldots,\vec{r}_A)\right]^\dagger e^{-i\vec{p}_\pi\cdot\vec{r}_1} \times \hat{\mathcal{S}}_{\pi N}(\vec{r}_1;\vec{r}_2,\ldots,\vec{r}_A) \times O_\mu(\vec{r}_1)\epsilon^\mu(\lambda)e^{i\vec{q}\cdot\vec{r}_1}\psi_A^{\text{g.s.}}(\vec{r}_1,\vec{r}_2,\ldots,\vec{r}_A). \quad (11)$$

We assume that $\hat{\mathcal{S}}_{N'N}$ and $\hat{\mathcal{S}}_{\pi N}$ are spin independent and that only elastic and mildly inelastic collisions with the spectator nucleons occur. The actual nuclear transparency measurements select events whereby the undetected final state with $(A-1)$ nucleons $|P_{A-1}^{\mu} J_R M_R\rangle$ is left with little excitation energy, which makes these assumptions very plausible. In computing the matrix element of Eq. (11) we consider processes of the type displayed in Fig. 1. The following spectator approximation is assumed to be valid for a struck nucleon with quantum numbers α_1:

$$\begin{aligned}
&\int d\vec{r}_1 \ldots \int d\vec{r}_A \{\phi_{\vec{p}_N}[P_n(\vec{r}_1)] \\
&\quad\times \hat{\mathcal{S}}_{N'N}^\dagger[P_n(\vec{r}_1);P_n(\vec{r}_2),\ldots,P_n(\vec{r}_A)] \\
&\quad\times \phi_{\alpha_2}[P_n(\vec{r}_2)]\ldots\phi_{\alpha_A}[P_n(\vec{r}_A)]\}^\dagger e^{-i\vec{p}_\pi\cdot\vec{r}_1} \\
&\quad\times \hat{\mathcal{S}}_{\pi N}(\vec{r}_1;\vec{r}_2,\ldots,\vec{r}_A)O_\mu(\vec{r}_1)e^{i\vec{q}\cdot\vec{r}_1}\phi_{\alpha_1}[P_m(\vec{r}_1)] \\
&\quad\times \phi_{\alpha_2}[P_m(\vec{r}_2)]\ldots\phi_{\alpha_A}[P_m(\vec{r}_A)] \\
&\approx \delta_{P_n(\vec{r}_2)P_m(\vec{r}_2)}\ldots\delta_{P_n(\vec{r}_A)P_m(\vec{r}_A)} \\
&\quad\times \int d\vec{r}_1 \ldots \int d\vec{r}_A \phi_{\vec{p}_N}^\dagger(\vec{r}_1)\hat{\mathcal{S}}_{N'N}[\vec{r}_1;P_n(\vec{r}_2),\ldots,P_n(\vec{r}_A)] \\
&\quad\times e^{-i\vec{p}_\pi\cdot\vec{r}_1}\hat{\mathcal{S}}_{\pi N}(\vec{r}_1;\vec{r}_2,\ldots,\vec{r}_A)O_\mu(\vec{r}_1)e^{i\vec{q}\cdot\vec{r}_1} \\
&\quad\times \phi_{\alpha_1}[P_m(\vec{r}_1)]\left|\phi_{\alpha_2}[P_m(\vec{r}_2)]\right|^2\ldots\left|\phi_{\alpha_A}[P_m(\vec{r}_A)]\right|^2, \quad (12)
\end{aligned}$$

with P_m and P_n permutations of the set $\{\vec{r}_1,\ldots,\vec{r}_A\}$ occurring in the antisymmetrization of the nucleon wave functions. Due to the presence of the δ functions, the right-hand side of Eq. (12) is nonvanishing under the condition that $P_m(\vec{r}_1)=\vec{r}_1$ and $P_m(\vec{r}_i)=P_n(\vec{r}_i)$ for $i=2,\ldots,A$. This means that both the bound wave function α_1 and the ejected nucleon have the same spatial coordinate as the operator, $\vec{r}_1$. Moreover, all $(A-1)!$ permutations of the subset $\{\vec{r}_2,\ldots,\vec{r}_A\}$ yield an identical right-hand side.

Thus, after expanding the wave functions in Eq. (11) and employing Eq. (12), we arrive at

$$\begin{aligned}
\mathcal{M}_{fi}^{(\gamma,N\pi)} \approx \frac{A(A-1)!}{A!}\int d\vec{r}_1 \int d\vec{r}_2 \ldots \int d\vec{r}_A \\
\times\left[|\phi_{\alpha_2}(\vec{r}_2)|^2\ldots|\phi_{\alpha_A}(\vec{r}_A)|^2 u^\dagger(\vec{p}_N,m_s)\right. \\
\times \hat{\mathcal{S}}_{\pi N}(\vec{r}_1;\vec{r}_2,\ldots,\vec{r}_A)\hat{\mathcal{S}}_{N'N}(\vec{r}_1;\vec{r}_2,\ldots,\vec{r}_A)\epsilon^\mu(\lambda) \\
\left.\times O_\mu(\vec{r}_1)e^{-i\vec{p}_m\cdot\vec{r}_1}\phi_{\alpha_1}(\vec{r}_1)\right]. \quad (13)
\end{aligned}$$

We now define the FSI factor $\mathcal{F}_{\text{FSI}}(\vec{r})$:

$$\begin{aligned}
\mathcal{F}_{\text{FSI}}(\vec{r}) = \int d\vec{r}_2 \ldots \int d\vec{r}_A \left|\phi_{\alpha_2}(\vec{r}_2)\right|^2\ldots\left|\phi_{\alpha_A}(\vec{r}_A)\right|^2 \\
\times \hat{\mathcal{S}}_{\pi N}(\vec{r};\vec{r}_2,\ldots,\vec{r}_A)\hat{\mathcal{S}}_{N'N}(\vec{r};\vec{r}_2,\ldots,\vec{r}_A), \quad (14)
\end{aligned}$$

and write

$$\begin{aligned}
\mathcal{M}_{fi}^{(\gamma,N\pi)} \approx \int d\vec{r}_1 \mathcal{F}_{\text{FSI}}(\vec{r}_1)u^\dagger(\vec{p}_N,m_s) \\
\times \epsilon^\mu(\lambda)O_\mu(\vec{r}_1)e^{-i\vec{p}_m\cdot\vec{r}_1}\phi_{\alpha_1}(\vec{r}_1). \quad (15)
\end{aligned}$$

In what follows, we assume that the pion production operator acts on a bound-state wave function as a scalar (factorization assumption): $O_\mu(\vec{r})\phi_{\alpha_1}(\vec{r}) \equiv \mathcal{C}_\mu\phi_{\alpha_1}(\vec{r})$. With

$$\phi_{\alpha_1}^D(\vec{p}) = \frac{1}{(2\pi)^{3/2}}\int d\vec{r}\, e^{-i\vec{p}\cdot\vec{r}}\phi_{\alpha_1}(\vec{r})\mathcal{F}^{\text{FSI}}(\vec{r}), \quad (16)$$

we can write

$$\mathcal{M}_{fi}^{(\gamma,N\pi)} \approx (2\pi)^{3/2}u^\dagger(\vec{p}_N,m_s)\epsilon^\mu(\lambda)\mathcal{C}_\mu\phi_{\alpha_1}^D(\vec{p}_m). \quad (17)$$

When studying nuclear transparencies, it is convenient to factorize the invariant matrix element such that it becomes a convolution of a factor describing the elementary pion photoproduction process and a factor modeling the combined effect of all FSI mechanisms of the outgoing hadrons. To reach this goal we relate the $\gamma + A \to (A-1) + N + \pi$ matrix element in Eq. (17) to the one for for free nucleons $\gamma + N_i \to N + \pi$

$$\left[\mathcal{M}_{fi\,\text{free}}^{(\gamma,N\pi)}\right]_{m_s,m_s'} = u^\dagger(\vec{p}_N,m_s)\epsilon^\mu(\lambda)\mathcal{C}_\mu u(\vec{p}_m,m_{s'}), \quad (18)$$

with $m_{s'}$ the spin of the initial nucleon. First, we consider the situation with vanishing FSI, second the more realistic case with inclusion of a FSI phase operator. When ignoring FSI, the wave functions for the ejected hadrons reduce to plane waves and $\mathcal{F}_{\text{FSI}}(\vec{r}) \equiv 1$, $\phi_{\alpha_1}^D(\vec{p}_m) \equiv \phi_{\alpha_1}(\vec{p}_m)$. After substituting in Eq. (17) the completeness relation for Dirac spinors:

$$\sum_{m_s'}\left[u(\vec{p}_m,m_s')\bar{u}(\vec{p}_m,m_s') - v(\vec{p}_m,m_s')\bar{v}(\vec{p}_m,m_s')\right] = \mathbb{1}_{4\times4}, \quad (19)$$

one obtains

$$\left[\mathcal{M}_{fi}^{(\gamma,N\pi)}\right]_{\text{RPWIA}} = (2\pi)^{3/2}\sum_{m_s'}\left[\mathcal{M}_{fi\,\text{free}}^{(\gamma,N\pi)}\right]_{m_s,m_s'}\bar{u}(\vec{p}_m,m_s') \times\phi_{\alpha_1}(\vec{p}_m) - \text{negative energy terms}, \quad (20)$$

where the RPWIA denotes the relativistic plane-wave impulse approximation. From this last expression it is clear that even with vanishing FSI the presence of negative-energy components makes factorization impossible. In what follows we neglect those terms:

$$\left[\mathcal{M}_{fi}^{(\gamma,N\pi)}\right]_{\text{RPWIA}} \approx (2\pi)^{3/2}\sum_{m_s'}\left[\mathcal{M}_{fi\,\text{free}}^{(\gamma,N\pi)}\right]_{m_s,m_s'}\bar{u}(\vec{p}_m,m_s')\phi_{\alpha_1}(\vec{p}_m). \quad (21)$$

The contraction of the Dirac spinor $\bar{u}$ with the bound nucleon wave function ϕ_{α_1} if negative-energy components are neglected is given by

$$\bar{u}(\vec{p}_m,m_s')\phi_{\alpha_1}(\vec{p}_m) = (-i)^l\sqrt{\frac{E_{N_i}(p_m)+m_{N_i}}{2m_{N_i}}}\alpha_{n\kappa}(p_m)\chi^\dagger_{\frac{1}{2},m_s'}\times\mathcal{Y}_{\kappa m}(\Omega_p,\vec{\sigma}), \quad (22)$$

where m_{N_i} is the free mass of the bound nucleon, $E_{N_i}(p_m) = \sqrt{m_{N_i}^2+p_m^2}$ and

$$\alpha_{n\kappa}(p_m) = \frac{2m_{N_i}}{E_{N_i}+m_{N_i}}g_{n\kappa}(p_m). \quad (23)$$

In this last equation $g_{n\kappa}$ is defined as

$$g_{n\kappa}(p) = i\sqrt{\frac{2}{\pi}}\int_0^\infty r^2dr\frac{G_{n\kappa(r)}}{r}j_l(pr), \quad (24)$$

with $j_l(pr)$ the spherical Bessel function of the first kind. After squaring the matrix element and summing over the quantum number m of the bound nucleon wave function, one can use the following property of the spin spherical harmonics $\mathcal{Y}_{\kappa m}$

$$\sum_m\mathcal{Y}_{\kappa m}(\Omega_p,\vec{\sigma})\mathcal{Y}^\dagger_{\kappa m}(\Omega_p,\vec{\sigma}) = \frac{(2j+1)}{8\pi}1\,\text{I}_{2\times2}. \quad (25)$$

Finally, by using $\chi^\dagger_{\frac{1}{2},m_s}\chi_{\frac{1}{2},m_s'} = \delta_{m_sm_s'}$, the free pion production process can be formally decoupled from the typical nuclear effects:

$$\overline{\sum_{fi}}|\mathcal{M}_{fi}^{(\gamma,N\pi)}|^2 = \frac{1}{2}\sum_{\lambda,m,m_s}|\mathcal{M}_{fi}^{(\gamma,N\pi)}|^2 \approx (2\pi)^3\frac{2j+1}{4\pi}\frac{E_{N_i}(p_m)+m_{N_i}}{2m_{N_i}}|\alpha_{n\kappa}(p_m)|^2 \times\frac{1}{4}\sum_{\lambda,m_s,m_s'}\left|\left[\mathcal{M}_{fi\,\text{free}}^{(\gamma,N\pi)}\right]_{m_s,m_s'}\right|^2. \quad (26)$$

The right-hand side of the above equation requires knowledge about the off-shell extrapolation of the pion photoproduction amplitude. For the on-shell situation, the matrix element for the pion photoproduction process can be linked to the cross section

$$\frac{1}{4}\sum_{\lambda,m_s,m_s'}\left|\left[\mathcal{M}_{fi\,\text{free}}^{(\gamma,N\pi)}\right]_{m_s,m_s'}\right|^2 \approx \frac{4\pi\left(s-m_{N_i}^2\right)^2}{m_{N_i}m_N}\frac{d\sigma^{\gamma\pi}}{d|t|}, \quad (27)$$

with $s = (p_N^\mu+p_\pi^\mu)^2$ and $t = (q^\mu-p_\pi^\mu)^2$ the Mandelstam variables of the free process. The off-shell extrapolation of Eq. (27) involves a correction due to the Fermi motion and the binding of the nucleon on which the photon is absorbed. This can be done in several different ways and it is not yet clear which of them are the most efficient and reliable. In this article, we consider photon energies $\geqslant$1.5 GeV that make off-shell corrections to s relatively small for typical nucleon momenta. For this reason, we deem it a reasonable approximation to adopt the Eq. (27) for sufficiently high photon energies.

After substituting Eqs. (26) and (27) in Eq. (1), the differential cross section for $\gamma+A\to(A-1)+N+\pi$ in the RPWIA reads

$$\left(\frac{d^5\sigma}{dE_\pi d\Omega_\pi d\Omega_N}\right)_{\text{RPWIA}} \approx \frac{M_{A-1}p_\pi p_N\left(s-m_{N_i}^2\right)^2}{4\pi m_{N_i}qE_A}f_{\text{rec}}^{-1}\frac{2j+1}{4\pi} \times\frac{\left[E_{N_i}(p_m)+m_{N_i}\right]}{2m_{N_i}}|\alpha_{n\kappa}(p_m)|^2\frac{d\sigma^{\gamma\pi}}{d|t|}. \quad (28)$$

When FSI are included, the derivation outlined earlier is no longer possible due to the presence of $\mathcal{F}_{\text{FSI}}(\vec{r})$ in ϕ_α^D. We define a distorted momentum distribution along the lines of Ref. [26]

$$\rho_D(\vec{p}_m) = \sum_{m_s,m}\left|\bar{u}(\vec{p}_m,m_s)\phi^D_{\alpha_1}(\vec{p}_m)\right|^2. \quad (29)$$

When FSI and negative-energy contributions to $\phi^D_{\alpha_1}$ are neglected, Eq. (29) reduces to $\frac{2j+1}{4\pi}\frac{E_{N_i}(p_m)+m_{N_i}}{2m_{N_i}}|\alpha_{n\kappa}(p_m)|^2$. Based on this analogy, we write the differential cross section with FSI as

$$\left(\frac{d^5\sigma}{dE_\pi d\Omega_\pi d\Omega_N}\right)_D \approx \frac{M_{A-1}p_\pi p_N\left(s-m_{N_i}^2\right)^2}{4\pi m_{N_i}qE_A}f_{\text{rec}}^{-1}\rho_D(\vec{p}_m)\frac{d\sigma^{\gamma\pi}}{d|t|}. \quad (30)$$

B. Pion electroproduction

The four-momentum of the virtual photon γ^* is $q^\mu(\omega,\vec{q})$ and the z axis lies along $\vec{q}$. The incoming (scattered) electron has four-momentum $p_e^\mu(E_e,\vec{p}_e)$ $[p_{e'}^\mu(E_{e'},\vec{p}_{e'})]$ and spin s (s'), θ_e denotes the electron scattering angle. With these additional notations and conventions, the differential cross section in the laboratory frame reads

$$\frac{d^8\sigma}{d\Omega_{e'}dE_{e'}dE_\pi d\Omega_\pi d\Omega_N} = \frac{m_e^2p_{e'}}{(2\pi)^3p_e}\frac{M_{A-1}m_Np_\pi p_N}{2(2\pi)^5E_A}f_{\text{rec}}^{-1}\overline{\sum_{fi}}|\mathcal{M}_{fi}^{(e,e'N\pi)}|^2, \quad (31)$$

with the recoil factor $f_{\rm rec}$ as in Eq. (2) and $\overline{\sum}_{fi}$ representing the averaging over initial electron spins and summing over the spins of the final particles. The invariant matrix element $\mathcal{M}_{fi}^{(e,e'N\pi)}$ can be written as

$$\mathcal{M}_{fi}^{(e,e'N\pi)} = \langle P_\pi^\mu, P_N^\mu m_s, P_{A-1}^\mu J_R M_R | j_\mu \frac{e}{Q^2} J^\mu | P_A^\mu 0^+ \rangle, \quad (32)$$

with the electron current

$$j_\mu = \bar{u}(\vec{p}_{e'}, s')\gamma_\mu u(\vec{p}_e, s), \quad (33)$$

$Q^2 = -q_\mu q^\mu$ and the hadron current J^μ. By defining an auxiliary current

$$a_\mu \equiv j_\mu - \frac{j_0}{\omega} q_\mu \quad (34)$$

and using current conservation, the following identity can readily be proved:

$$j_\mu J^\mu = -a_i J_i = -a_i \delta_{ij} J_j = -\sum_{\lambda=(x,y,z)} a_i e_i(\lambda) e_j(\lambda) J_j, \quad (35)$$

where $\vec{e}(\lambda)$ is the unit vector along the axis $\lambda = (x, y, z)$. After defining the electron density matrix

$$\rho_{\lambda\lambda'} = \sum_{ss'} \left[\vec{e}(\lambda)\cdot\vec{a}\right]^\dagger \left[\vec{e}(\lambda')\cdot\vec{a}\right] \quad (36)$$

and the hadronic matrix elements

$$w_\lambda = \langle P_\pi^\mu, P_N^\mu m_s, P_{A-1}^\mu J_R M_R | \vec{e}(\lambda)\cdot\vec{J} | P_A^\mu 0^+ \rangle, \quad (37)$$

we can write for the matrix element

$$\sum_{ss'} |\mathcal{M}_{fi}^{(e,e'N\pi)}|^2 = \frac{e^2}{Q^4} \sum_{\lambda\lambda'} \rho_{\lambda\lambda'} w_\lambda^\dagger w_{\lambda'}. \quad (38)$$

With the degree of transverse polarization defined as

$$\epsilon = \left(1 + \frac{2q^2}{Q^2}\tan^2\frac{\theta_e}{2}\right)^{-1}, \quad (39)$$

the electron density matrix becomes [27]

$$\rho_{\lambda\lambda'} = \frac{Q^2}{m_e^2}\frac{1}{1-\epsilon} \times \begin{bmatrix} \frac{1}{2}(1+\epsilon) & 0 & -\frac{1}{2}\sqrt{2\frac{Q^2}{\omega^2}\epsilon(1+\epsilon)} \\ 0 & \frac{1}{2}(1-\epsilon) & 0 \\ -\frac{1}{2}\sqrt{2\frac{Q^2}{\omega^2}\epsilon(1+\epsilon)} & 0 & \frac{Q^2}{\omega^2}\epsilon \end{bmatrix}. \quad (40)$$

After substituting Eq. (40) in Eq. (38), one can factor out a part containing all the variables related to the electrons in the differential cross section:

$$\frac{d^8\sigma}{d\Omega_{e'} dE_{e'} dE_\pi d\Omega_\pi d\Omega_N} = \Gamma \frac{d^5\sigma_v}{dE_\pi d\Omega_\pi d\Omega_N} \equiv \Gamma \mathcal{C} \overline{\sum} |\mathcal{M}_{fi}^{(\gamma^*,N\pi)}|^2. \quad (41)$$

Here, $\mathcal{M}_{fi}^{(\gamma^*,N\pi)} = \langle P_\pi^\mu, P_N^\mu m_s, P_{A-1}^\mu J_R M_R | \hat{\mathcal{O}} | q^\mu, P_A^\mu 0^+ \rangle$, $\mathcal{C} = \frac{M_{A-1} m_N p_\pi p_N}{4(2\pi)^5 E_\gamma E_A} f_{\rm rec}^{-1}$, and $\Gamma = \frac{\alpha}{2\pi^2}\frac{E_{e'}}{E_e}\frac{E_\gamma}{Q^2}\frac{1}{1-\epsilon}$ is the electron flux factor, with the virtual photon equivalent energy $E_\gamma = \frac{s-M_A^2}{2M_A}$, the fine-structure constant α, and $s = (q^\mu + P_A^\mu)^2$ the Mandelstam variable of the virtual photoproduction process. The cross section can be cast in the following form

$$\frac{d^5\sigma_v}{dE_\pi d\Omega_\pi d\Omega_N} \equiv \frac{d^5\sigma_T}{dE_\pi d\Omega_\pi d\Omega_N} + \epsilon\frac{d^5\sigma_L}{dE_\pi d\Omega_\pi d\Omega_N} + \epsilon\frac{d^5\sigma_{TT}}{dE_\pi d\Omega_\pi d\Omega_N} + \sqrt{\epsilon(\epsilon+1)}\frac{d^5\sigma_{TL}}{dE_\pi d\Omega_\pi d\Omega_N}, \quad (42)$$

with

$$\begin{aligned} \frac{d^5\sigma_T}{dE_\pi d\Omega_\pi d\Omega_N} &= \frac{\mathcal{C}}{2}\sum_{m_s M_R}(|J_x|^2 + |J_y|^2), \\ \frac{d^5\sigma_L}{dE_\pi d\Omega_\pi d\Omega_N} &= \mathcal{C}\frac{Q^2}{\omega^2}\sum_{m_s M_R}|J_z|^2, \\ \frac{d^5\sigma_{TT}}{dE_\pi d\Omega_\pi d\Omega_N} &= \frac{\mathcal{C}}{2}\sum_{m_s M_R}(|J_x|^2 - |J_y|^2), \\ \frac{d^5\sigma_{TL}}{dE_\pi d\Omega_\pi d\Omega_N} &= \frac{-\mathcal{C}}{2}\sqrt{\frac{2Q^2}{\omega^2}}\sum_{m_s M_R}(J_x^* J_z + J_z^* J_x). \end{aligned} \quad (43)$$

As for the photoproduction case, we wish to establish a relation between the invariant matrix element for virtual-photon pion production on a nucleus ($\mathcal{M}_{fi}^{(\gamma^*,N\pi)}$) and on a free nucleon ($\mathcal{M}_{fi,\rm free}^{(\gamma^*,N\pi)}$). In comparison with the real photoproduction process, the virtual photon has an extra degree of polarization and $Q^2 \neq 0$. This does not alter the derivation presented in the previous subsection and after neglecting negative energy contributions, one arrives at

$$\mathcal{M}_{fi}^{(\gamma^*,N\pi)} \approx (2\pi)^{3/2}\sum_{m_{s'}} \left(\mathcal{M}_{fi,\rm free}^{(\gamma^*,N\pi)}\right)_{\lambda,m_s,m_{s'}} \bar{u}(\vec{p}_m, m_{s'})\phi_\alpha^D(\vec{p}_m). \quad (44)$$

The matrix element $\mathcal{M}_{fi,\rm free}^{(\gamma^*,N\pi)}$ is related to the free electroproduction process by

$$\frac{d^5\sigma^{eN}}{dE_{e'}d\Omega_{e'}d\phi_\pi^* d|t|} = \Gamma' \frac{m_N^2}{2(2\pi)^2\left(s'-m_N^2\right)^2}\overline{\sum}|\mathcal{M}_{fi,\rm free}^{(\gamma^*,N\pi)}|^2, \quad (45)$$

where $\Gamma' = \frac{\alpha}{2\pi^2}\frac{E_{e'}}{E_e}\frac{K}{Q^2}\frac{1}{1-\epsilon}$ is the electron flux factor, with the virtual photon equivalent energy $K = \frac{s'-m_N^2}{2m_N}$. Further, $s' = (p_N^\mu + p_\pi^\mu)^2$ and $t = (q^\mu - p_\pi^\mu)^2$ are the Mandelstam variables for the free process. Starred variables denote center-of-mass values.

With $\rho_{\rm D}$ defined in Eq. (29) and by making use of Eqs. (44) and (45), we arrive at the factorized form for the differential $A(e, e'N\pi)$ cross section:

$$\left(\frac{d^8\sigma}{d\Omega_{e'}dE_{e'}dE_\pi d\Omega_\pi d\Omega_N}\right)_{\rm D} = \frac{\Gamma}{\Gamma'}\frac{M_{A-1}p_N p_\pi\left(s'-m_N^2\right)^2}{2m_N E_\gamma E_A} f_{\rm rec}^{-1}\rho_{\rm D}\frac{d^5\sigma^{eN}}{dE_{e'}d\Omega_{e'}d|t|d\phi_\pi^*}. \quad (46)$$

We wish to stress that the assumptions made to arrive at this expression are essentially identical to those made for the real photon case discussed in the previous subsection.

C. Final-state interactions

The Glauber approach can be justified when the wavelength of the outgoing hadron is sufficiently small in comparison to the typical interaction length with the residual nucleons. In the context of $A(e, e'p)$ reactions [28] it was shown that the Glauber model represents a realistic approach to FSI for proton kinetic energies down to about 300 MeV. This corresponds to proton de Broglie wavelengths of the order of 1.5 fm. For pions comparable wavelengths are reached for kinetic energies of the order of 700 MeV.

A relativistic extension of the Glauber model, dubbed the relativistic multiple-scattering Glauber approximation (RMSGA), was introduced in Ref. [24]. In the RMSGA, the wave function for the ejected nucleon and pion is a convolution of a relativistic plane wave and an Glauber eikonal phase operator that accounts for FSI mechanisms. In Glauber theory the assumption is made that a fast-moving particle interacts through elastic or mildly inelastic collisions with *frozen* point scatterers in a target. Scattering angles are assumed small and each of the point scatterers adds a phase to the wave function, resulting in the following expression for the Glauber eikonal phase:

$$\widehat{\mathcal{S}}_{iN}(\vec{r}, \vec{r}_2, \ldots, \vec{r}_A) = \prod_{j=2}^{A}[1 - \Gamma_{iN}(\vec{b} - \vec{b}_j)\theta(z_j - z)] \quad (\text{with} \quad i = \pi \quad \text{or} \quad N'). \tag{47}$$

Here, $\vec{r}_j(\vec{b}_j, z_j)$ are the coordinates of the residual nucleons and $\vec{r}(\vec{b}, z)$ specifies the interaction point with the (virtual) photon. In Eq. (47), the z axis lies along the path of the ejected particle i (the proton or pion) and $\vec{b}$ is perpendicular to this path. The Heaviside step function θ guarantees that only nucleons in the forward path of the outgoing particle contribute to the eikonal phase.

Reflecting the diffractive nature of the nucleon-nucleon ($N'N$) and pion-nucleon (πN) collisions at intermediate energies, the profile functions $\Gamma_{N'N}$ and $\Gamma_{\pi N}$ in Eq. (47) are parametrized as

$$\Gamma_{iN}(\vec{b}) = \frac{\sigma_{iN}^{\text{tot}}(1 - i\epsilon_{iN})}{4\pi\beta_{iN}^2} \exp\left(-\frac{\vec{b}^2}{2\beta_{iN}^2}\right) \quad (\text{with } i = \pi \text{ or } N'). \tag{48}$$

Here, the parameters σ_{iN}^{tot} (total cross section), β_{iN} (slope parameter), and ϵ_{iN} (ratio of the real to imaginary part of the scattering amplitude) depend on the momentum of the outgoing nucleon or pion i. For $i = N'$, we determined the parameters by performing a fit [24] to the $N'N \longrightarrow N'N$ databases from the Particle Data Group (PDG) [29]. For the pion, $\sigma_{\pi N}^{\text{tot}}$ was fitted to data collected by PDG [29]. The analysis of the slope parameter in Ref. [30] was used for the $\beta_{\pi N}$ fits. Fits provided by SAID [31,32] and data from

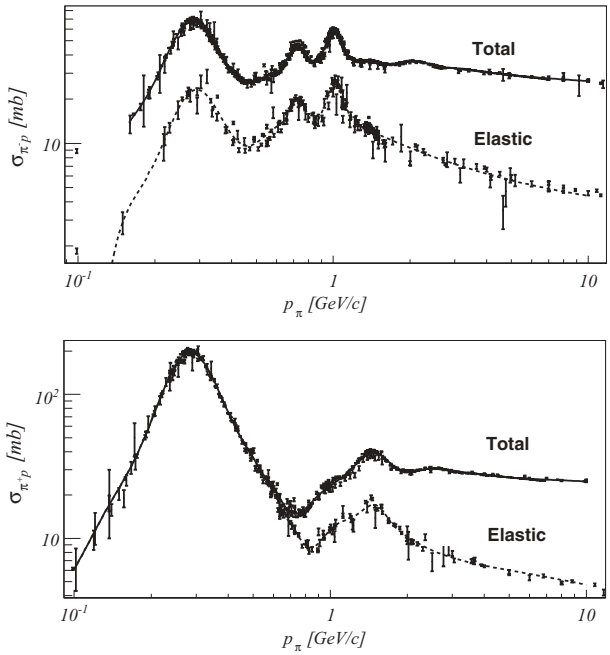

FIG. 2. The pion lab-momentum dependence of the data [29] and adopted fits for the total and elastic cross section for π^--p (upper panel) and π^+-p (lower panel) scattering.

PDG [29] were used in constructing the fits for $\epsilon_{\pi N}$. The fits for σ_{iN}^{tot}, β_{iN}, and ϵ_{iN} of Figs. 2, 3, and 4 are the result of a χ^2 minimization of the data against a a n-th degree polynomial (with $n \leqslant 10$). An alternative way of determining $\beta_{\pi N}$, is via

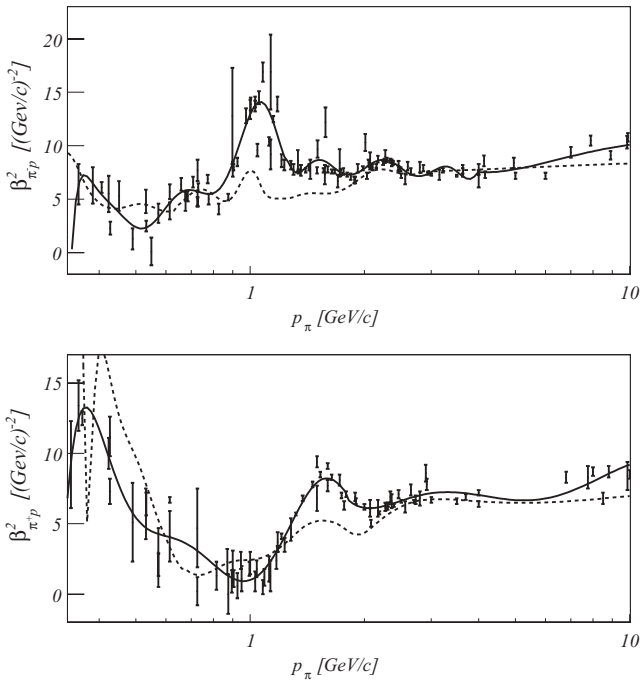

FIG. 3. The pion lab-momentum dependence of the data [30] and fits for the $\beta^2_{p\pi}$ parameter for π^--p (upper panel) and π^+-p (lower panel) scattering. Full curves are a χ^2 fit to the data, whereas the dashed curves result from Eq. (49).

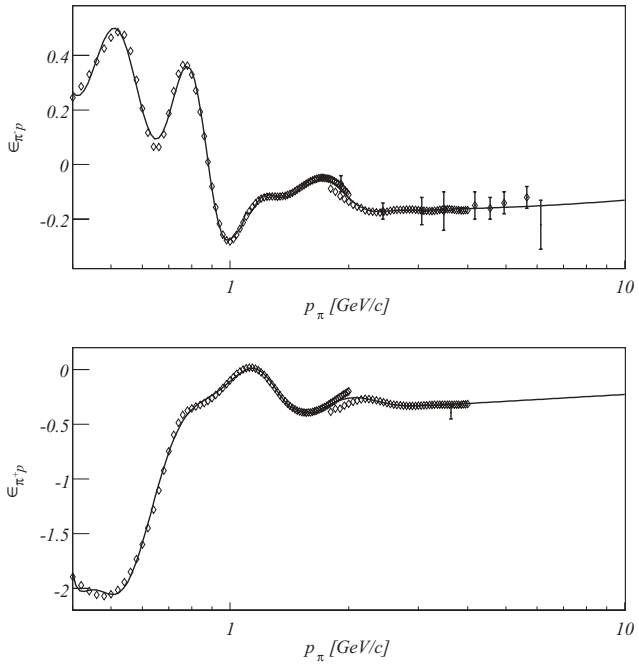

FIG. 4. The pion lab-momentum dependence of the ratio of the real to imaginary part of the $\pi^- p$ (upper panel) and $\pi^+ p$ (lower panel) amplitudes. The diamonds represent an analysis of the data by the George Washington University group [31,32], whereas the solid circles are from PDG [29]. The solid line is the fit to the data that are used in the numerical calculations.

the relation

$$\beta_{\pi N}^2 = \frac{\left(\sigma_{\pi N}^{\rm tot}\right)^2\left(1+\epsilon_{\pi N}^2\right)}{16\pi\,\sigma_{\pi N}^{\rm el}}, \tag{49}$$

with $\sigma_{\pi N}^{\rm el}$ the elastic cross section. Fits for $\sigma_{\pi N}^{\rm el}$ to data from PDG [29] are also presented in Fig. 2. The two sets for the $\beta_{\pi N}$ parameter in Fig. 3 do not produce significantly different results for the numerical calculations presented here. We use the χ^2 fit for $\beta_{\pi N}$ in all calculations presented in this article.

The Glauber operator of Eq. (47) is an A-body operator. As a consequence, it requires integrations over all spectator nucleon coordinates in Eq. (14), which is computationally very demanding, in particular for heavy target nuclei. In $\gamma^{(*)} + A \to (A-1) + N + \pi$ calculations, a product of two Glauber phases is involved and the cylindrical symmetry of the individual phases is lost. A Romberg algorithm is used to perform the integrations over the spatial coordinates in Eq. (14).

For nucleons with a kinetic energy lower than about 300 MeV, the approximations underlying the Glauber formalism are no longer applicable, and an alternative method to model FSI is required. Under those circumstances our framework provides the flexibility to adopt the relativistic optical model eikonal approximation (ROMEA) [33]. In the ROMEA approach, the wave function of a nucleon with energy $E = \sqrt{p_N^2 + m_N^2}$ after scattering in a scalar $[V_s(r)]$ and vector $[V_v(r)]$ spherical potential has the following form:

$$\psi^{(+)}_{\vec{p}_N, m_s}(\vec{r}) = \sqrt{\frac{E+m_n}{2m_N}}\left[\frac{1}{\frac{1}{E+m_N+V_s(r)-V_v(r)}\vec{\sigma}\cdot\hat{\vec{p}}}\right] e^{i\vec{p}_N\cdot\vec{r}} e^{i\hat{\mathcal{S}}_{N'N}(\vec{r})}\chi_{\frac{1}{2}m_s}, \tag{50}$$

with the eikonal phase determined by

$$i\hat{\mathcal{S}}_{N'N}(\vec{b},z) = -i\frac{m_N}{K}\int_{-\infty}^{z} dz'\{V_c(\vec{b},z') + V_{\rm so}(\vec{b},z') \times [\vec{\sigma}\cdot(\vec{b}\vec{K}) - iKz']\}. \tag{51}$$

In this last equation, $\vec{K} = \frac{1}{2}(\vec{k}_i + \vec{k}_f)$ is the average of the initial and final momentum of the scattering particle. In the small angle approximation, $\vec{K} \approx \vec{p}_N$ and points along the z axis. The central and spin-orbit potentials V_c and V_{so} are functions of V_s and V_v and their derivatives [33].

Additional approximations were used in the implementation of optical-potential FSI in this ROMEA model. The dynamical enhancement of the lower components of the scattering wave function (50) is ignored as at low momenta the lower components are small compared to the upper components due to $\hat{\vec{p}}$ and at higher momenta $(V_s - V_v)$ is small in comparison to $(E + m_N)$. The operator $\hat{\vec{p}}$ was also substituted by the asymptotic value $\vec{p}_N$. Finally, as collisions were assumed spin independent in Eq. (12), the spin-orbit potential V_{so} in Eq. (51) is neglected. This yields the following phase factor entering in Eq. (14):

$$\hat{\mathcal{S}}^{\rm ROMEA}_{N'N}(\vec{r}) = e^{-i\frac{m_N}{p_N}\int_{z_N}^{+\infty} dz V_c(\vec{b}_{p_N}, z)}. \tag{52}$$

In contrast to the Glauber eikonal phase, the optical potential eikonal phase of Eq. (52) depends solely on the coordinate $\vec{r}$ that defines the interaction point. As a consequence, it can be taken out of all the integrations in Eq. (14) and the cylindrical symmetry of the pion Glauber eikonal factor is retained, hereby considerably reducing the cost of computing the total FSI factor $\mathcal{F}_{\rm FSI}$. For the numerical evaluation of the ROMEA phase factor, we made use of the optical potential of van Oers *et al.* [34] for ^{4}He and the global $(S-V)$ parametrization of Cooper *et al.* [35] for heavier nuclei.

D. Color transparency and short-range correlations

We implement color transparency effects in the usual fashion by replacing the total cross sections $\sigma_{iN}^{\rm tot}$ in the profile functions of Eq. (48) with effective ones [36]. The latter induce some reduced pion-nucleon and nucleon-nucleon interaction over a typical length scale l_h corresponding with the hadron formation length $(i = \pi \,{\rm or}\, N')$

$$\frac{\sigma_{iN}^{\rm eff}}{\sigma_{iN}^{\rm tot}} = \left\{\left[\frac{\mathcal{Z}}{l_h} + \frac{\langle n^2 k_t^2\rangle}{\mathcal{H}}\left(1-\frac{\mathcal{Z}}{l_h}\right)\right]\theta(l_h-\mathcal{Z}) + \theta(\mathcal{Z}-l_h)\right\}. \tag{53}$$

Here, n is the number of elementary fields (2 for the pion, 3 for the nucleon), $k_t = 0.350\,{\rm GeV/c}$ is the average transverse momentum of a quark inside a hadron, $\mathcal{Z}$ is the distance from the interaction point, and $l_h \simeq 2p/\Delta M^2$ is the hadronic

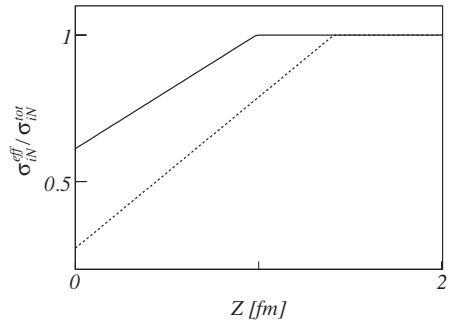

FIG. 5. Comparison of the CT effect on the total effective cross section $\sigma_{iN}^{\rm eff}$ for nucleon-nucleon (full) and pion-nucleon (dashed) interactions. We consider the situation whereby the ejectile possesses a lab momentum of 2.5 GeV/c. For the hard-scale parameter we adopt $\mathcal{H} = 1.8\,(\mathrm{GeV}/c)^2$.

expansion length, with p the momentum of the final hadron and ΔM^2 the mass squared difference between the intermediate prehadron and the final hadron state. We adopt the values $\Delta M^2 = 1\,\mathrm{GeV}^2$ for the proton and $\Delta M^2 = 0.7\,\mathrm{GeV}^2$ for the pion. $\mathcal{H}$ is the hard-scale parameter that governs the CT effect. It equals the momentum transfer $t = (q^\mu - p_\pi^\mu)^2$ (pion CT) or $u = (q^\mu - p_N^\mu)^2$ (nucleon CT) for pion photoproduction and Q^2 for pion electroproduction. Figure 5 illustrates the predicted difference of the CT effect on the pion-nucleon and nucleon-nucleon effective interaction. Reflecting its mesonic nature, the pion has a longer formation length and during its formation its interaction cross section with the residual nucleons is more strongly reduced than for a nucleon.

We now proceed with introducing a method that allows us to implement the effect of SRC in the relativistic Glauber calculations. The proposed method adopts the thickness approximation as a starting point. In the thickness approximation, the density $|\phi_{\alpha_i}(\vec{r}_i)|^2$ of the individual nucleons in Eq. (14) is replaced by an averaged density $\rho_A^{[1]}(\vec{r})$ defined as

$$\rho_A^{[1]}(\vec{r}) = A \int d\vec{r}_2 \ldots \int d\vec{r}_A \left[\psi_A^{\rm g.s.}(\vec{r}, \vec{r}_2, \ldots, \vec{r}_A)\right]^\dagger \times \psi_A^{\rm g.s.}(\vec{r}, \vec{r}_2, \ldots, \vec{r}_A). \quad (54)$$

In terms of $\rho_A^{[1]}(\vec{r})$ the FSI factor of Eq. (14) can be approximated by

$$\mathcal{F}_{\rm FSI}^{\rm thick}(\vec{r}) = \frac{1}{A^{A-1}} \int d\vec{r}_2 \ldots \int d\vec{r}_A \rho_A^{[1]}(\vec{r}_2)\rho_A^{[1]}(\vec{r}_3)\ldots\rho_A^{[1]}(\vec{r}_A) \times \hat{\mathcal{S}}_{\pi N}(\vec{r}; \vec{r}_2, \ldots, \vec{r}_A)\hat{\mathcal{S}}_{N'N}(\vec{r}; \vec{r}_2, \ldots, \vec{r}_A). \quad (55)$$

In combination with the operators of Eq. (47) the expression can be further simplified to

$$\mathcal{F}_{\rm FSI}^{\rm thick}(\vec{r}) = \left\{ \int d\vec{r}_2 \frac{\rho_A^{[1]}(\vec{r}_2)}{A} [1 - \Gamma_{N'p}(\vec{b}_{N'} - \vec{b}_{N'2})\theta(z_{N'2} - z_{N'})] \times [1 - \Gamma_{\pi p}(\vec{b}_\pi - \vec{b}_{\pi 2})\theta(z_{\pi 2} - z_\pi)] \right\}^{Z - \frac{\tau_z+1}{2}} \times \left\{ \int d\vec{r}_3 \frac{\rho_A^{[1]}(\vec{r}_3)}{A} [1 - \Gamma_{N'n}(\vec{b}_{N'} - \vec{b}_{N'3})\theta(z_{N'3} - z_{N'})] \times \theta[1 - \Gamma_{\pi n}(\vec{b}_\pi - \vec{b}_{\pi 3})(z_{\pi 3} - z_\pi)] \right\}^{N + \frac{\tau_z - 1}{2}}, \quad (56)$$

where τ_z is the isospin (1 for protons and -1 for neutrons) of the nucleon on which the initial absorption took place. The $z_{N'}$ (z_π) axis lies along the ejected nucleon (pion). The above expression is derived within the context of the IPM. It is clear that the nucleus has a fluid nature and that the IPM can only be considered as a first-order approximation. In computing the FSI effects by means of the Eq. (56) one fails to give proper attention to one important piece of information: namely that one considers the density distribution of nucleons given that there is one present at the photointeraction point $\vec{r}$.

The two-body density $\rho_A^{[2]}(\vec{r}_1, \vec{r}_2)$ is related to the probability to find a nucleon at position $\vec{r}_2$ given that there is one at a position $\vec{r}_1$. We adopt the following normalization convention for $\rho_A^{[2]}$

$$\int d\vec{r}_1 \int d\vec{r}_2 \rho_A^{[2]}(\vec{r}_1, \vec{r}_2) = A(A-1). \quad (57)$$

In the IPM on has $[\rho_A^{[2]}(\vec{r}_1, \vec{r}_2)]_{\rm IPM} \equiv \frac{A-1}{A}\rho_A^{[1]}(\vec{r}_1)\rho_A^{[1]}(\vec{r}_2)$. The nucleus has a granular structure as the nucleons have a finite size. This gives rise to strong nucleon-nucleon repulsions at short internucleon distances that reflect themselves in SRC at the nuclear scale. One can correct $[\rho_A^{[2]}(\vec{r}_1, \vec{r}_2)]$ for the presence of the SRC by adopting the following functional form [37]

$$\rho_A^{[2]}(\vec{r}_1, \vec{r}_2) \equiv \gamma(\vec{r}_1)\left[\rho_A^{[2]}(\vec{r}_1, \vec{r}_2)\right]_{\rm IPM}\gamma(\vec{r}_2)g(r_{12}) = \frac{A-1}{A}\gamma(\vec{r}_1)\rho_A^{[1]}(\vec{r}_1)\rho_A^{[1]}(\vec{r}_2)\gamma(\vec{r}_2)g(r_{12}), \quad (58)$$

with $g(r_{12})$ the so-called Jastrow correlation function and $\gamma(\vec{r})$ a function that imposes the normalization condition of Eq. (57) on $\rho_A^{[2]}(\vec{r}_1, \vec{r}_2)$. The function $\gamma(\vec{r})$ is a solution to the following integral equation

$$\gamma(\vec{r}_1) \int d\vec{r}_2 \rho_A^{[1]}(\vec{r}_2)g(r_{12})\gamma(\vec{r}_2) = A, \quad (59)$$

which can be solved numerically. The Glauber phase factor of Eq. (56) can now be corrected for SRC through the following substitution

$$\rho_A^{[1]}(\vec{r}_2) \to \frac{A}{A-1}\frac{\rho_A^{[2]}(\vec{r}_2, \vec{r})}{\rho_A^{[1]}(\vec{r})} = \gamma(\vec{r}_2)\rho_A^{[1]}(\vec{r}_2)\gamma(\vec{r})g(|\vec{r}_2 - \vec{r}|) \equiv \rho_A^{\rm eff}(\vec{r}_2, \vec{r}), \quad (60)$$

whereby $\rho_A^{[2]}(\vec{r}_2, \vec{r})$ adopts the expression (58). These manipulations amount to the following final expression for the Glauber FSI factor including SRC:

$$\mathcal{F}_{\rm FSI}^{\rm SRC}(\vec{r}) = \left\{ \int d\vec{r}_2 \frac{\gamma(\vec{r}_2)\rho_A^{[1]}(\vec{r}_2)\gamma(\vec{r})g(|\vec{r}_2 - \vec{r}|)}{A} \times [1 - \Gamma_{N'p}(\vec{b}_{N'} - \vec{b}_{N'2})\theta(z_{N'2} - z_{N'})] \times [1 - \Gamma_{\pi p}(\vec{b}_\pi - \vec{b}_{\pi 2})\theta(z_{\pi 2} - z_\pi)] \right\}^{Z - \frac{\tau_z+1}{2}}$$

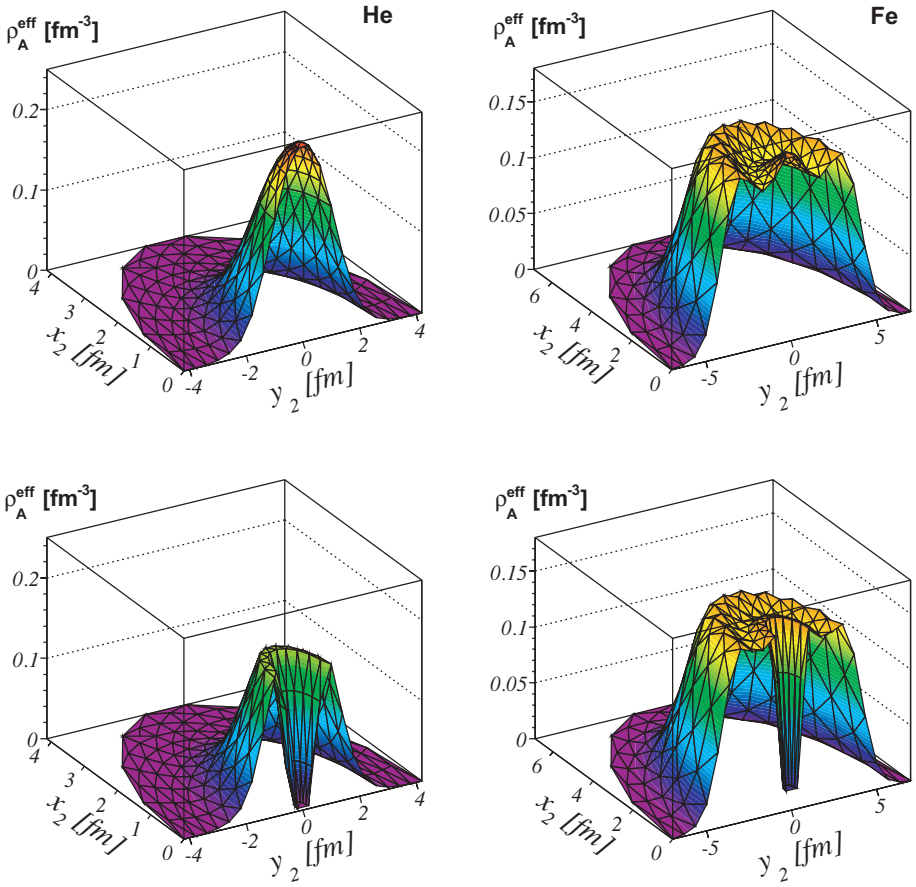

FIG. 6. (Color online) The effective nuclear density $\rho_A^{\rm eff}(\vec{r}_2, \vec{r})$ at $z_2 = 0$ for He (left) and Fe (right) before (upper) and after (lower panel) the inclusion of SRC effects. The effective nuclear densities here refer to the situation whereby the (virtual) photon is absorbed at the origin ($x = 0$, $y = 0$, $z = 0$).

$$\times \left\{ \int d\vec{r}_3 \frac{\gamma(\vec{r}_3)\rho_A^{[1]}(\vec{r}_3)\gamma(\vec{r})g(|\vec{r}_3 - \vec{r}|)}{A} \right.$$
$$\times [1 - \Gamma_{N'n}(\vec{b}_{N'} - \vec{b}_{N'3})\theta(z_{N'3} - z_{N'})]$$
$$\left. \times [1 - \Gamma_{\pi n}(\vec{b}_\pi - \vec{b}_{\pi 3})\theta(z_{\pi 3} - z_\pi)] \right\}^{N + \frac{\tau_z - 1}{2}} . \quad (61)$$

The effective density of Eq. (60) accounts for the fact that the motion of each nucleon does depend on the presence of the other ones. In Fig. 6 we display the effective nuclear density as it would be observed by a nucleon or a pion created after photoabsorption on a nucleon at the center of the nucleus. The figure shows the density for Fe as computed in the IPM [$\rho_A^{[1]}(x, y, z \equiv 0)$] and with the expression based on the substitution of Eq. (60)

$$\gamma(x, y, z \equiv 0)\rho_A^{[1]}(x, y, z \equiv 0)\gamma(x \equiv 0, y \equiv 0, z \equiv 0)g(|\vec{r}|).$$

In Fig. 6 and all forthcoming numerical calculations we use a correlation function $g(|\vec{r}|)$ from Ref. [38]. It is characterized by a (Gaussian) hard core of about 0.8 fm and a second bump that extends to internucleon distances r of about 2 fm and reaches its maximum for $r_{12} \approx 1.3$ fm. This correlation function provided a fair description of the SRC contributions to ^{12}C$(e, e'pp)$ [39] and ^{16}O$(e, e'pp)$ [40]. It is clear that the SRC lead to a local reduction—with size of the nucleon radius—of the density around the nucleon struck by the (virtual) photon. To preserve the proper normalization, this reduction amounts to some enhanced density at distances of about twice the nucleon radius. With regard to the intranuclear attenuation, the reduction of the density in the proximity of the struck nucleon will result in some enhanced transparency close to the photointeraction point $\vec{r}$. The enhanced density at positions of about twice the nucleon radius from the struck nucleon, can be expected to have the opposite effect.

III. NUMERICAL RESULTS

A. The FSI factor

In this subsection we present a selected number of results of the numerical calculations of the RMSGA FSI factor of Eq. (14). We consider the ^{12}C$(\gamma, p\pi^-)$ reaction in a reference frame with the z axis along the momentum $\vec{p}_N$ of the ejected nucleon and the y axis along $\vec{p}_\pi \times \vec{p}_N$ (with $\vec{p}_\pi$ in the lower hemisphere). In what follows, $\theta_{N\pi}$ stands for the angle of the pion relative to the nucleon. It has a negative value in all calculations considered in this section. The coordinate $\vec{r}$ denotes the interaction point with the external photon. We present the FSI factor versus the spherical coordinates in this frame.

In Fig. 7, we present the calculated norm and phase of the FSI factor in the scattering plane ($\phi = 0$) for $p_N \approx 2.6$ GeV and $p_\pi \approx 2.3$ GeV, which are conditions for which Jefferson Lab collected data. We present the FSI factor for the proton

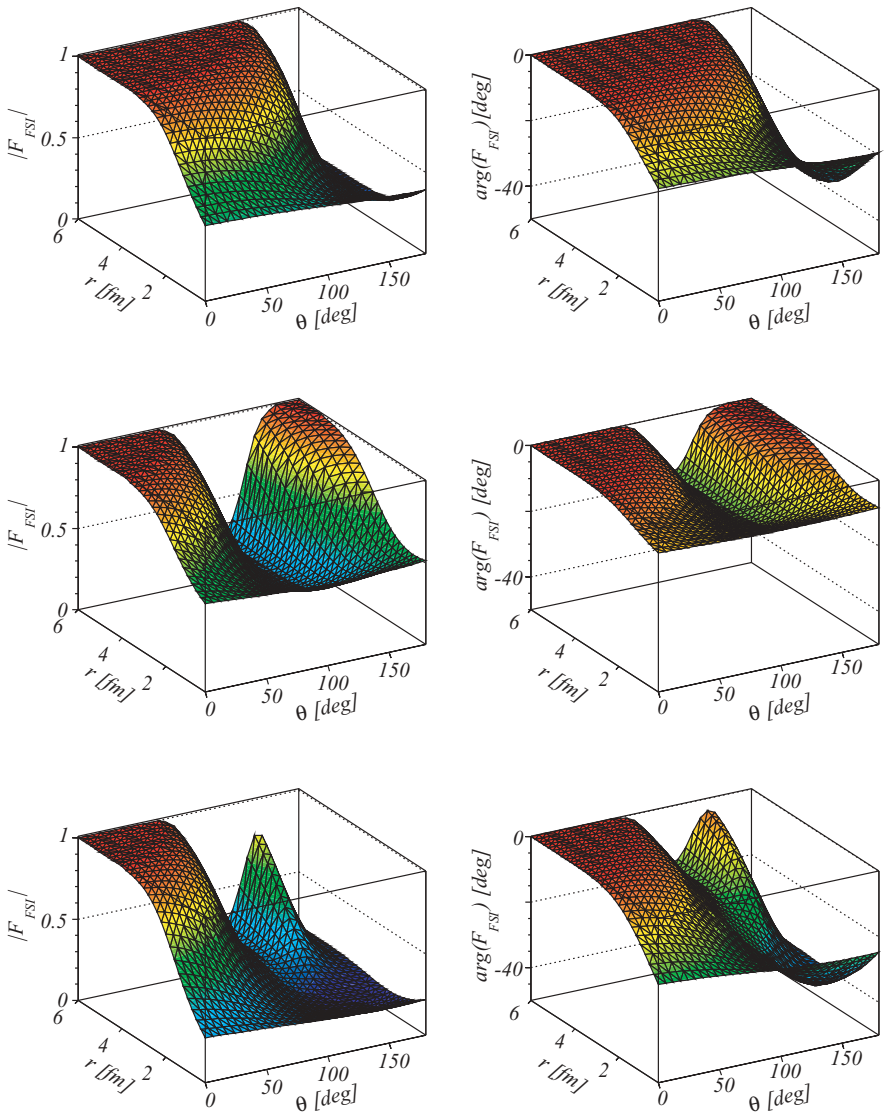

FIG. 7. (Color online) Radial and polar-angle dependence of the norm (left) and phase (right) of the FSI factor $\mathcal{F}_{\rm FSI}$ in the scattering plane ($\phi = 0^\circ$) for the ^{12}C(γ, $p\pi^-$) reaction from the $1s_{1/2}$ level. For the upper (middle) panels, solely the FSI effects on the ejected proton (pion) are considered. The lower panels include the net effect of both the pion and nucleon FSI effect. The results are obtained for $p_N = 2638$ MeV, $p_\pi = 2291$ MeV, and $\theta_{N\pi} = -65.19^\circ$.

and the pion separately as well as the combined effect when the two are detected in coincidence.

When looking at the θ dependence, it becomes clear from Fig. 7 that the norm is smallest in the direction opposite the momentum of the particle (being 180° for the nucleon and $180^\circ + \theta_{N\pi}$ for the pion). For these directions and large r, the nucleon or pion is created close to the surface of the nucleus on the opposite side of its asymptotic direction and has to travel through a thick layer of nuclear medium before it reaches a free status. As for the r dependence, we see for the nucleon a reduction of the FSI effects for rising r at angles in the neighborhood of $\theta = 0^\circ$ and, respectively, an increment for rising r at $\theta = 180^\circ$. This is again due to the fact that the outgoing nucleon traverses less, respectively; more nuclear matter on its way out of the nucleus. The same observations apply for the pion, albeit at the angles $\theta_{N\pi}$ and $180^\circ + \theta_{N\pi}$. The total FSI factor combines the intranuclear attenuation effects on the nucleon and pion. Hence, the norm shows the largest reduction at θ around 180° and $180^\circ + \theta_{N\pi}$. The phase of the FSI factor exhibits similar behavior, with the largest phase shifts occurring at the discussed angles.

Figure 8 teaches us a couple things about the ϕ dependence of the FSI factor. As the outgoing nucleon lies along the z axis there is no dependence on the azimuthal angle because of the cylindrical symmetry. Again, we can see that the absorption is largest when large amounts of nuclear matter need to be traversed (i.e., large θ). Looking at the pion we see the largest attenuation occurs in the upper hemisphere ($\cos\phi \geqslant 0$) as a pion that is created in this region has to traverse the inner core of the nucleus. The combined effect of the pion and nucleon contributions is contained in the bottom panel. As the reaction takes place in the xz plane, the total FSI factor retains the following symmetry: $\mathcal{F}_{\rm FSI}(r, \theta, \phi) = \mathcal{F}_{\rm FSI}(r, \theta, 2\pi - \phi)$.

B. Pion photoproduction

The experiment E94-104 at Jefferson Lab extracted nuclear transparencies for $\gamma + {}^4\mathrm{He} \rightarrow p + \pi^- + {}^3\mathrm{He}$. The measurements were performed for photon energies $1.6 \leqslant q \leqslant 4.2$ GeV and for $\theta_{\rm c.m.} = 70^\circ$ and 90°, with $\theta_{\rm c.m.}$ the center-of-mass angle between the photon and pion. In total, the nuclear transparencies were measured for eight kinematical settings.

TABLE I. Central values for the photon energy (MeV), proton momentum p_N (MeV), proton angle θ_N, pion momentum p_π (MeV), and pion angle θ_π for $\theta_{\text{c.m.}} = 70^\circ, 90^\circ$. Angles are measured relative to the incoming photon momentum.

q	$\theta_{\text{c.m.}}$	p_N	θ_N	p_π	θ_π
1648	70°	989	47.39°	1238	−36.02°
1648	90°	1277	37.37°	1015	−47.73°
2486	70°	1322	44.37°	1794	−31.02°
2486	90°	1740	34.45°	1438	−43.18°
3324	70°	1642	41.74°	2363	−27.56°
3324	90°	2195	32.01°	1866	−38.57°
4157	70°	1949	39.51°	2929	−25.05°
4157	90°	2638	30.01°	2291	−35.18°
4327	70°	2011	39.1°	3044	−24.6°
4327	90°	2727	29.6°	2377	−34.6°
5160	70°	2307	37.3°	3606	−22.8°
5160	90°	3161	28.0°	2797	−32.1°
6059	70°	2622	35.6°	4211	−21.2°
6059	90°	3625	26.6°	3250	−29.9°
7025	70°	2956	33.9°	4861	−19.8°
7025	90°	4120	25.2°	3735	−28.0°
8057	70°	3309	32.4°	5555	−18.6°
8057	90°	4646	24.0°	4253	−26.3°
9156	70°	3683	31.0°	6294	−17.6°
9156	90°	5204	22.8°	4805	−24.8°
10322	70°	4077	29.7°	7077	−16.6°
10322	90°	5794	21.8°	5389	−23.5°

In a proposal for a follow-up experiment, seven additional kinematics are suggested for measurements at higher photon energies and $\theta_{\text{c.m.}} = 90^\circ$ [41]. We have performed calculations for the completed and planned experiments. Table I provides a list of the kinematics.

We aim at performing calculations that match the kinematic conditions of the experiment as closely as possible. We use the following definition for the transparency:

$$T = \frac{\sum_\alpha \int dq\, Y(q) \int d\vec{p}_m \left(\frac{d^5\sigma}{dE_{\pi_i} d\Omega_{\pi_i} d\Omega_{N_i}}\right)_{\text{RMSGA}}}{\sum_\alpha \int dq\, Y(q) \int d\vec{p}_m \left(\frac{d^5\sigma}{dE_{\pi_i} d\Omega_{\pi_i} d\Omega_{N_i}}\right)_{\text{RPWIA}}}. \quad (62)$$

The integrations $\int dq \int d\vec{p}_m$ in Eq. (62) were evaluated with a random integration algorithm. To this end, random events within the photon beam energy range, detector acceptances, and applied cuts for each data point were generated for the calculation of the transparency until convergence of the order of 5% was reached. Typically, this involves about 1000 events for each data point. In Eq. (62), $\sum_\alpha$ extends over all occupied single-particle states in the target nucleus. All cross sections are computed in the laboratory frame. $Y(q)$ provides the weight factor for the generated events. It includes the yield of the reconstructed experimental photon beam spectrum [14] for the photon energy of the generated event. We assume that the elementary $\gamma + n \to \pi^- + p$ cross section $\frac{d\sigma^{\gamma\pi}}{d|t|}$ in Eqs. (28) and (30) remains constant over the kinematical ranges $\int dq \int d\vec{p}_m$ that define a particular data point. With this assumption the cross section $\frac{d\sigma^{\gamma\pi}}{d|t|}$ cancels out of the ratio (62). For all kinematic conditions of Table I, the pion and nucleon momenta are sufficiently high for the RMSGA method to be a valid approach for describing the FSI mechanism.

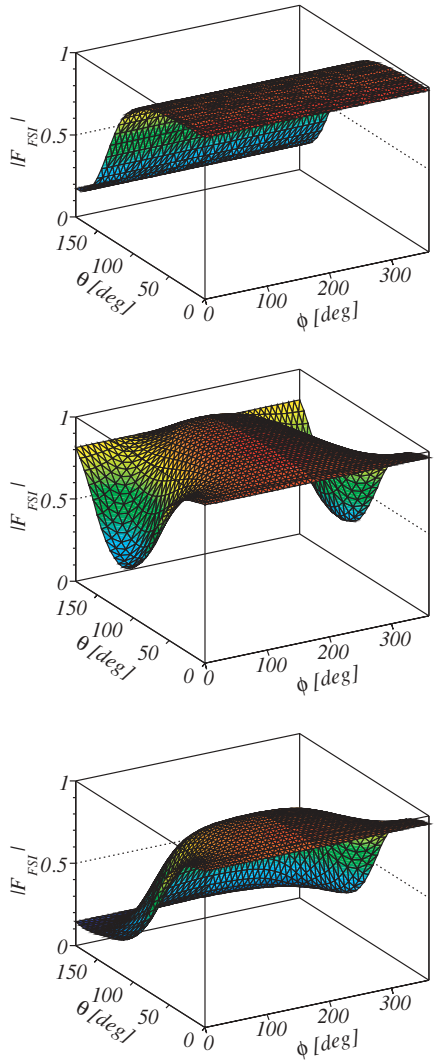

FIG. 8. (Color online) Polar- and azimuthal-angle dependence of the norm of the FSI factor $\mathcal{F}_{\text{FSI}}$ at a distance $r = 3$ fm from the center of the nucleus for the $^{12}\text{C}(\gamma, p\pi^-)$ reaction from the $1s_{1/2}$ level. Separate contributions from the nucleon (upper panel) and the pion (middle panel), as well as their combined effect (bottom panel), are shown. Kinematics as in Fig. 7.

For a discussion of the computed results compared to the experimental data and a semi-classical model we refer the reader to Ref. [17]. In Fig. 9 the separated transparencies for the outgoing proton and pion are displayed next to the full result. It is clear from this figure that the rise of the transparency at low $|t|$ can be attributed to the proton contribution. This rise can be attributed to the local minimum in the total nucleon-nucleon cross section for nucleon momenta of about 1 GeV.

Figure 9 also shows that the ^{4}He nucleus is more transparent for pion emission than for proton emission. This can be partially attributed to the lower pion total cross sections. As pointed out in Fig. 5 the larger formation length and corresponding bigger reduction of the effective cross section make that the CT effect is larger for pions than for protons.

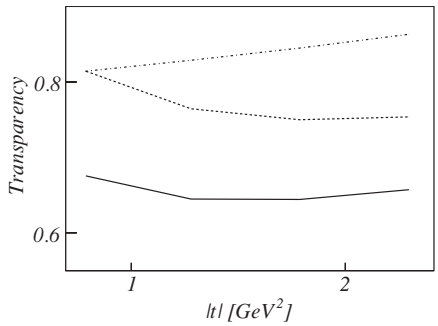

FIG. 9. Contributions of the pion (dashed-dotted) and nucleon (dashed) to the total nuclear transparency (full) extracted from ^{4}He(γ, $p\pi^-$) versus $|t|$ at $\theta_{\text{c.m.}} = 70^\circ$. All calculations include CT.

In Fig. 10 the computed increase in the nuclear transparency caused by CT and SRC mechanisms is shown as a function of $|t|$. One observes that SRC mechanisms increase the nuclear transparency by about 5%. As there is no direct dependence on the hard scale, the increase is almost independent of $|t|$. The CT phenomenon, however, shows a linear rise from almost 0 to over 20% at the largest values of $|t|$. For $-t \leqslant 2.5$ GeV^2 the predicted effect of SRC is larger than the increase induced by the CT mechanism. The SRC decrease the slope in the $-t$ dependence of the CT phenomenon. Indeed, the SRC induces holes in the nuclear density in the direct neighborhood of the interaction point (see Fig. 6) where the CT effects are largest. At high $|t|$ the short-range correlations have a modest impact on the magnitude of the CT effects. Our investigations show that by studying the hard-scale dependence of the transparency the CT-related mechanisms can be clearly separated from the SRC ones.

In the search of phenomena like CT in transparency studies, it is of the utmost importance to possess robust and advanced calculations based on concepts from traditional nuclear physics. Thereby, one of the major sources of uncertainty stem from the description of FSI mechanisms. In our eikonal model, we can either use optical potentials (ROMEA) or a Glauber framework (RMSGA). In kinematic regions of moderate hadron momenta both approaches can be used [28]. As they adopt very different underlying assumptions, we consider a comparison between the predictions of the two approaches as a profound test of the trustworthiness of either approach. We computed the transparency of the ^{4}He(γ, $p\pi^-$) reaction for kinematics at $\theta_{\text{c.m.}} = 70^\circ$ and 90° with ejected proton momenta ranging from 500 MeV/c to 1 GeV/c. As can be appreciated from Fig. 11, both descriptions yield a similar shape, but the RMSGA calculations are consistently larger by about 5%. At higher nucleon momenta, however, the difference between the predictions for the transparencies in the two approaches shrinks to a few percentages. The estimated model dependence in the computed transparencies is of the same order as the predicted role of SRC mechanisms. From these observations, it is clear that pion and nuclear transparencies are not the optimum observables to study SRC mechanisms in nuclei. Indeed they bring about a relatively modest overall renormalization of about 5%. Unlike the CT effects, for example, their role does not grow with an increasing hard scale, nor is there any sizable A dependence in the SRC effects.

TABLE II. Central values of Q^2 (GeV^2), incoming electron energy E_e (MeV), electron scattering angle θ_e (degrees), scattered electron energy $E_{e'}$ (MeV), ejected pion momentum p_π (MeV), and ejected pion angle (degrees) for the kinematics of the Jefferson Laboratory experiment E01-107. Angles are measured relative to the incoming electron beam.

Q^2	E_e	θ_e	$E_{e'}$	p_π	θ_π
1.10	4021	27.76°	1190	2793	10.58°
2.15	5012	28.85°	1730	3187	13.44°
3.00	5012	37.77°	1430	3418	12.74°
3.91	5767	40.38°	1423	4077	11.53°
4.69	5767	52.67°	1034	4412	9.09°

C. Pion electroproduction

The E01-107 collaboration at Jefferson Lab measured the nuclear transparency for the pion electroproduction process on H, ^{12}C, ^{27}Al, ^{64}Cu, and ^{197}Au. Measurements were done for the kinematics listed in Table II. In all the measurements the pion

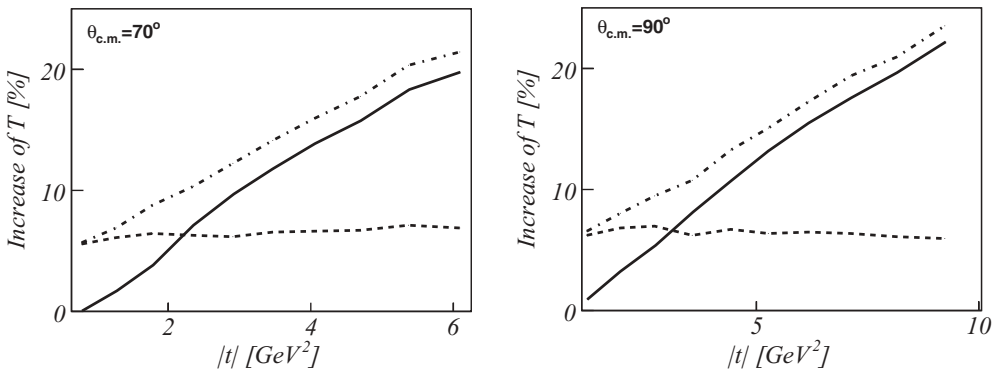

FIG. 10. The $|t|$ dependence of the relative increase of the nuclear transparency due to SRC and CT effects. We consider the ^{4}He(γ, $p\pi^-$) reaction at $\theta_{\text{c.m.}} = 70^\circ$ (left panel) and 90° (right panel) and kinematic conditions from Table I. The baseline result is the RMSGA calculation. The solid (dashed) curve includes the effect of CT (SRC). The dot-dashed line is the combined effect of CT+SRC.

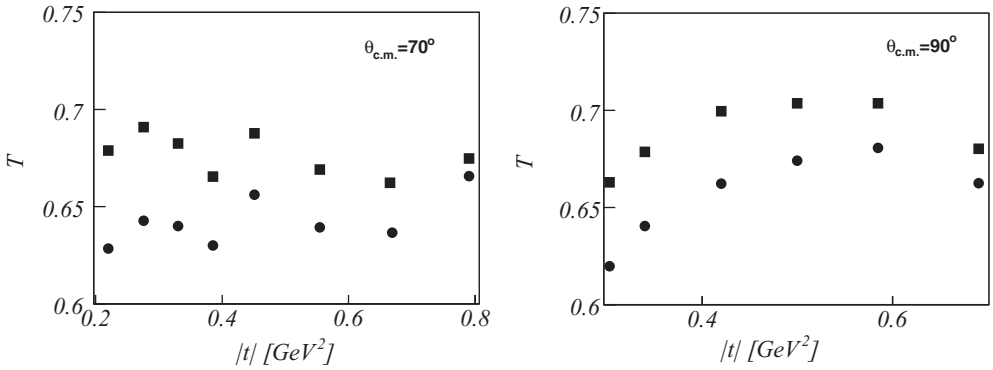

FIG. 11. Comparison between the RMSGA (squares) and ROMEA (circles) description of the nucleon transparency of the ^{4}He(γ, $p\pi^-$) reaction for kinematics at $\theta_{\text{c.m.}} = 70^\circ$ (left panel) and 90° (right panel). Neither CT nor SRC effects were included in the calculations.

is detected in a relatively narrow cone about the momentum transfer. We have performed calculations for all target nuclei. The transparency is defined as

$$T = \frac{\sum_\alpha \int d\omega Y(\omega) \int_{\Delta^3 p_m} d\vec{p}_m \left(\frac{d^8\sigma}{d\Omega_{e'} dE_{e'} dE_\pi d\Omega_\pi d\Omega_N}\right)_{\text{RMSGA}}}{\sum_\alpha \int d\omega Y(\omega) \int_{\Delta^3 p_m} d\vec{p}_m \left(\frac{d^8\sigma}{d\Omega_{e'} dE_{e'} dE_\pi d\Omega_\pi d\Omega_N}\right)_{\text{RPWIA}}}. \quad (63)$$

The integration over ω takes into account the spread in energy of the virtual photon in the experiment and weighs each point with the reconstructed yield $Y(\omega)$ [42]. The quantity $\Delta^3 p_m$ specifies the phase space of the missing momentum and is determined by the condition $|p_m| \leqslant 300$ MeV/c and the experimental cuts and detector acceptances. An experimental cut of 100 MeV was placed on the missing mass of the final state. Accordingly, the undetected final neutron is an extremely slow one. The experimentally determined

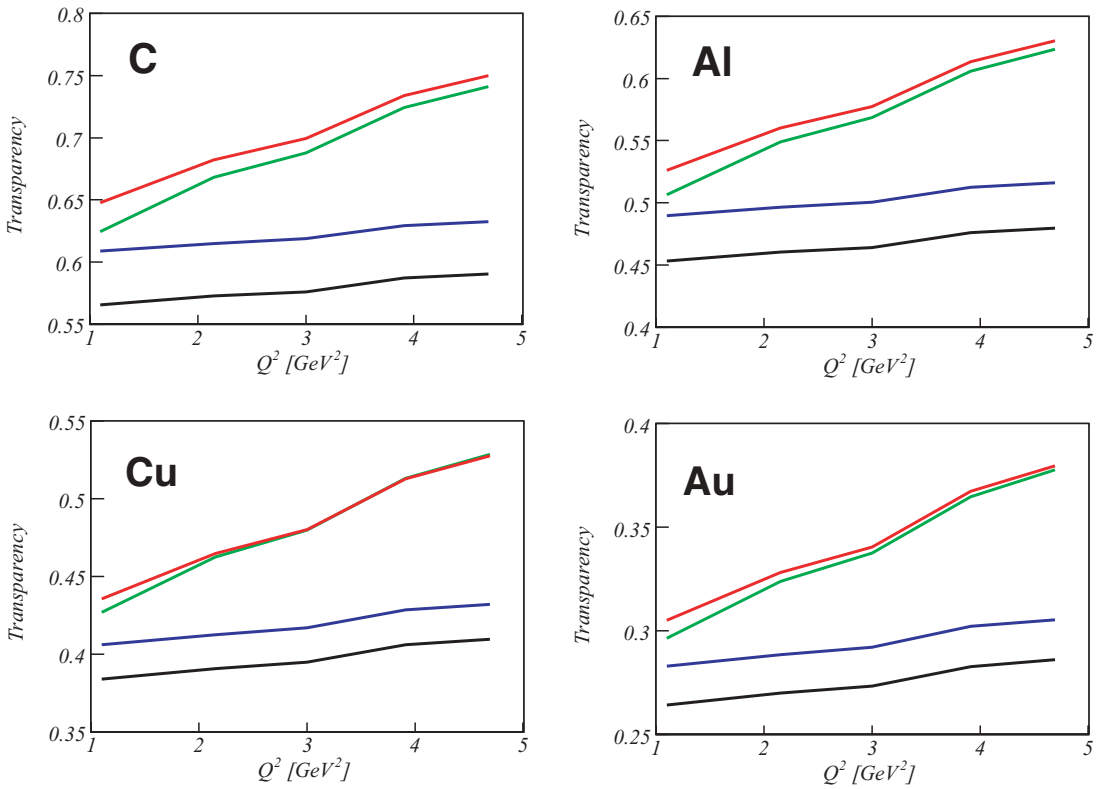

FIG. 12. (Color online) The Q^2 dependence of the nuclear transparency for the $A(e, e'\pi^+)$ process in ^{12}C,^{27}Al,^{63}Cu, and ^{197}Au. The black and green curves are RMSGA and RMSGA+CT calculations respectively. The blue and red line are RMSGA+SRC and RMSGA+SRC+CT results.

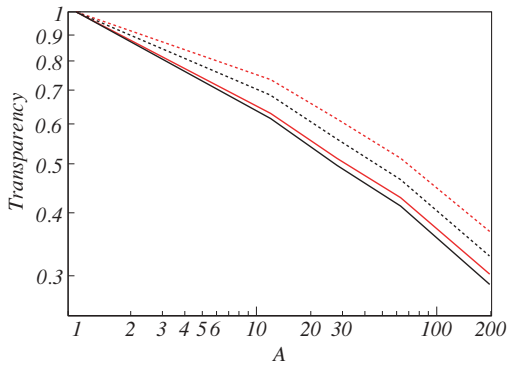

FIG. 13. (Color online) A dependence of the transparency for the $A(e, e'\pi^+)$ process at $Q^2 = 1.1\,\mathrm{GeV}^2$ (black) and $Q^2 = 4.69\,\mathrm{GeV}^2$ (red). The solid curves denote RMSGA+SRC results. The dashed lines are RMSGA+CT+SRC calculations.

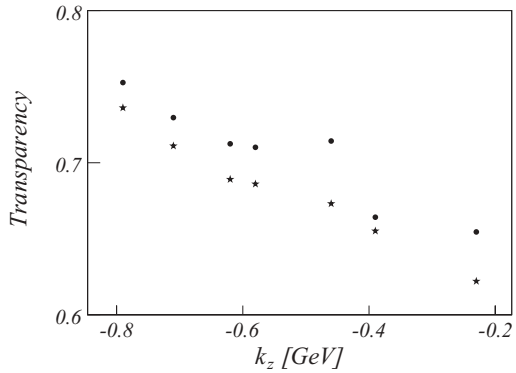

FIG. 14. Nuclear transparency results for $^{12}\mathrm{C}(e, e'\pi^+)$ versus the z component of $\vec{k} = \vec{p}_\pi - \vec{q}$ for kinematics corresponding to data points of the JLab experiment of Ref. [15]. The circles are RMSGA+CT predictions, whereas the stars are from the semiclassical calculations of Ref. [16].

transparency was formed by dividing the measured yield by a Monte Carlo equivalent yield for the targets with nucleon number A and comparing it to the ratio of the yields from the ^{1}H target [15]. As the Monte Carlo simulation does not include the attenuation mechanisms on the detected pions, the measured transparency is a measure of these. We compute these intranuclear attenuation effects on the ejected pions in the RMSGA model. Thereby, we use a parametrization provided by the E01-107 collaboration for the free electroproduction in Eq. (46) [42,43].

Figure 12 presents the results from our transparency calculations for the electroproduction reaction. The RMSGA calculations show a modest increase over the Q^2 range. This behavior finds a simple explanation in the p_π dependence of the $\sigma^{\mathrm{tot}}_{\pi^+ p}$ of Fig. 2. The results contained in Fig. 12 cover a range in pion momenta given by $2.8 \leqslant p_\pi \leqslant 4.4$ GeV. In this range, $\sigma^{\mathrm{tot}}_{\pi^+ p}$ displays a soft decrease, which reflects itself in a soft increase of the nuclear transparency. The RMSGA+CT transparencies are again about 5% larger than the RMSGA ones. The RMSGA+CT shows a strong Q^2 dependence with CT-related enhancements up to 20% at the highest energies. The evolution of the A dependence of the transparency is shown in Fig. 13. One observes that the addition of CT to the calculation adds more curvature and that this increases with higher Q^2. Finally, in Fig. 14, we compare our model calculations with the results from the semiclassical model of Ref. [16]. The transparency is plotted as function of $\vec{k} = \vec{p}_\pi - \vec{q}$. As in the photoproduction calculations [17], our results again turn out to be higher by a few percentages.

IV. CONCLUSION

We have outlined a relativistic framework to compute nuclear transparencies in exclusive $A(\gamma, N\pi)$ and $A(e, e'N\pi)$ reactions. For the bound states, the model uses relativistic mean-field wave functions. At sufficiently high nucleon and pion energies, the intranuclear attenuation on the ejected particles can be computed with a relativistic version of the Glauber model. At lower ejectile energies, the framework offers the flexibility to use optical potentials. For nucleon momenta where both approaches can be applied, the Glauber and optical-potential based calculations predict nucleon transparencies in ^{4}He that follow similar trends. The differences in the magnitude of the transparency is smaller than 5% and shrinks with nucleon momentum. Our RMSGA predictions for the pion transparencies are in reasonable agreement with the semiclassical results of Larson, Miller, and Strikman. Both models predict similar trends, with the RMSGA predictions being systematically ≈5% higher. This provides support that the baseline nuclear-physics transparencies can be computed in a rather model-independent fashion. Extension of our relativistic and quantum mechanical photoproduction calculations up to energies accessible in the JLab 12 GeV upgrade show an increase of the transparency up to 20% at the highest energies due to color transparency. Transparencies are also enhanced through the inclusion of SRC effects in the calculations. This yields an increase of about 5%, independent of the hard scale. Accordingly the SRC and CT mechanisms can be clearly separated.

[1] A. S. Carroll *et al.*, Phys. Rev. Lett. **61**, 1698 (1988).
[2] I. Mardor *et al.*, Phys. Rev. Lett. **81**, 5085 (1998).
[3] A. Leksanov *et al.*, Phys. Rev. Lett. **87**, 212301 (2001).
[4] J. L. S. Aclander *et al.*, Phys. Rev. C **70**, 015208 (2004).
[5] G. Garino *et al.*, Phys. Rev. C **45**, 780 (1992).
[6] N. Makins *et al.*, Phys. Rev. Lett. **72**, 1986 (1994).
[7] T. G. O'Neill *et al.*, Phys. Lett. **B351**, 87 (1995).
[8] D. Abbott *et al.*, Phys. Rev. Lett. **80**, 5072 (1998).
[9] K. Garrow *et al.*, Phys. Rev. C **66**, 044613 (2002).
[10] D. Dutta *et al.* (Jefferson Lab E91013), Phys. Rev. C **68**, 064603 (2003).
[11] M. R. Adams *et al.* (E665), Phys. Rev. Lett. **74**, 1525 (1995).
[12] A. Airapetian *et al.* (HERMES), Phys. Rev. Lett. **90**, 052501 (2003).

[13] E. M. Aitala *et al*. (E791), Phys. Rev. Lett. **86**, 4773 (2001).
[14] D. Dutta *et al*. (Jefferson Lab E940104), Phys. Rev. C **68**, 021001 (2003).
[15] B. Clasie *et al*., Phys. Rev. Lett. **99**, 242502 (2007).
[16] A. Larson, G. A. Miller, and M. Strikman, Phys. Rev. C **74**, 018201 (2006).
[17] W. Cosyn, M. C. Martínez, J. Ryckebusch, and B. Van Overmeire, Phys. Rev. C **74**, 062201(R) (2006).
[18] H. Gao, R. J. Holt, and V. R. Pandharipande, Phys. Rev. C **54**, 2779 (1996).
[19] N. N. Nikolaev *et al*., Phys. Lett. **B317**, 281 (1993).
[20] S. Frankel, W. Frati, and N. R. Walet, Phys. Rev. C **51**, R1616 (1995).
[21] M. Alvioli, C. Ciofi degli Atti, and H. Morita, Fizika B**13**, 585 (2004).
[22] R. J. Furnstahl, B. D. Serot, and H.-B. Tang, Nucl. Phys. **A615**, 441 (1997).
[23] W. Greiner, *Relativistic Quantum Mechanics: Wave Equations* (Springer-Verlag, Berlin, 2000).
[24] J. Ryckebusch, D. Debruyne, P. Lava, S. Janssen, B. Van Overmeire, and T. Van Cauteren, Nucl. Phys. **A728**, 226 (2003).
[25] F. X. Lee, T. Mart, C. Bennhold, and L. E. Wright, Nucl. Phys. **A695**, 237 (2001).
[26] J. R. Vignote, M. C. Martinez, J. A. Caballero, E. Moya de Guerra, and J. M. Udias, Phys. Rev. C **70**, 044608 (2004).
[27] F. X. Lee, C. Bennhold, and L. E. Wright, Phys. Rev. C **55**, 318 (1997).
[28] P. Lava, M. C. Martínez, J. Ryckebusch, J. A. Caballero, and J. M. Udias, Phys. Lett. **B595**, 177 (2004).
[29] W.-M. Yao, C. Amsler, D. Asner, R. Barnett, J. Beringer, P. Burchat, C. Carone, C. Caso, O. Dahl, G. D'Ambrosio *et al*., J. Phys. G **33**, 1 + (2006), http://pdg.lbl.gov.
[30] T. Lasinski, R. Levi Setti, B. Schwarzschild, and P. Ukleja, Nucl. Phys. **B37**, 1 (1972).
[31] R. A. Arndt, W. J. Briscoe, I. I. Strakovsky, R. L. Workman, and M. M. Pavan, Phys. Rev. C **69**, 035213 (2004).
[32] R. L. Workman (private communication, 2005).
[33] B. Van Overmeire, W. Cosyn, P. Lava, and J. Ryckebusch, Phys. Rev. C **73**, 064603 (2006).
[34] W. T. H. van Oers *et al*., Phys. Rev. C **25**, 390 (1982).
[35] E. D. Cooper, S. Hama, B. C. Clark, and R. L. Mercer, Phys. Rev. C **47**, 297 (1993).
[36] G. R. Farrar, H. Liu, L. L. Frankfurt, and M. I. Strikman, Phys. Rev. Lett. **61**, 686 (1988).
[37] S. Frankel, W. Frati, and N. Walet, Nucl. Phys. **A580**, 595 (1994).
[38] C. Gearhart, Ph. D. thesis, Washington University, 1994.
[39] K. I. Blomqvist *et al*., Phys. Lett. **B421**, 71 (1998).
[40] J. Ryckebusch and W. Van Nespen, Eur. Phys. J. A **20**, 435 (2004).
[41] D. Dutta (private communication, 2006).
[42] B. Clasie (private communication, 2006).
[43] T. Horn, Ph. D. thesis, University of Maryland, 2006.